AIP | Physics of Plasmas

Resistive magnetohydrodynamic reconnection: Resolving long-term, chaotic dynamics

R. Keppens, O. Porth, K. Galsgaard, J. T. Frederiksen, A. L. Restante, G. Lapenta, and C. Parnell

Citation: Physics of Plasmas (1994-present) **20**, 092109 (2013); doi: 10.1063/1.4820946
View online: http://dx.doi.org/10.1063/1.4820946
View Table of Contents: http://scitation.aip.org/content/aip/journal/pop/20/9?ver=pdfcov
Published by the AIP Publishing

Resistive magnetohydrodynamic reconnection: Resolving long-term, chaotic dynamics

R. Keppens,[1] O. Porth,[2] K. Galsgaard,[3] J. T. Frederiksen,[3] A. L. Restante,[1] G. Lapenta,[1] and C. Parnell[4]
[1]*Centre for mathematical Plasma-Astrophysics, Department of Mathematics, KU Leuven, Belgium*
[2]*Department of Applied Mathematics, The University of Leeds, Leeds LS2 9JT, United Kingdom*
[3]*The Niels Bohr Institute, University of Copenhagen, København K, Denmark*
[4]*School of Mathematics and Statistics, University of St. Andrews, Fife, United Kingdom*

(Received 7 June 2013; accepted 19 August 2013; published online 13 September 2013)

In this paper, we address the long-term evolution of an idealised double current system entering reconnection regimes where chaotic behavior plays a prominent role. Our aim is to quantify the energetics in high magnetic Reynolds number evolutions, enriched by secondary tearing events, multiple magnetic island coalescence, and compressive versus resistive heating scenarios. Our study will pay particular attention to the required numerical resolutions achievable by modern (grid-adaptive) computations, and comment on the challenge associated with resolving chaotic island formation and interaction. We will use shock-capturing, conservative, grid-adaptive simulations for investigating trends dominated by both physical (resistivity) and numerical (resolution) parameters, and confront them with (visco-)resistive magnetohydrodynamic simulations performed with very different, but equally widely used discretization schemes. This will allow us to comment on the obtained evolutions in a manner irrespective of the adopted discretization strategy. Our findings demonstrate that all schemes used (finite volume based shock-capturing, high order finite differences, and particle in cell-like methods) qualitatively agree on the various evolutionary stages, and that resistivity values of order 0.001 already can lead to chaotic island appearance. However, none of the methods exploited demonstrates convergence in the strong sense in these chaotic regimes. At the same time, nonperturbed tests for showing convergence over long time scales in ideal to resistive regimes are provided as well, where all methods are shown to agree. Both the advantages and disadvantages of specific discretizations as applied to this challenging problem are discussed.
 [http://dx.doi.org/10.1063/1.4820946]

I. INTRODUCTION

Magnetic reconnection is a key process in plasma physics, and early models based on stationary resistive magnetohydrodynamic (MHD)[1,2] considerations have played a prominent role in many follow-up investigations. The use of steady-state arguments to predict trends in reconnection behavior under varying plasma beta, magnetic Reynolds number, and other relevant parameters still continues to provide clear estimates for reconnection rates, outflow velocities, and diffusion region aspect ratios.[3,4] These recent studies also serve as examples where compressibility enters the analysis, an aspect which has also been incorporated in single fluid resistive MHD simulations which extend the analysis to up-down asymmetric setups.[5] Compressibility is also a key in 2D visco-resistive MHD studies which demonstrated that Petschek-like reconnection can be achieved with spatially uniform resistivity, when a tailored viscosity prescription is used.[6] These augment the large body of knowledge already obtained in dedicated collaborative modelling challenges, with the Geospace Environment Modelling (GEM) magnetic reconnection challenge[7] and the related Newton challenge[8] as prime examples. In both these challenges, the nonlinear evolution of a 2D setup was computed and compared with a code parc spanning single fluid resistive MHD up to full kinetic particle in cell (PIC) treatments. They categorise as non-driven to driven scenarios and indicated how at least a Hall-MHD prescription with a minimal decoupling between electron and ion dynamics were required for obtaining faster reconnection rates. In the Newton (driven) reconnection challenge comparison, resistive MHD computations with anomalously raised resistivity prescriptions could also rival the rates found in extended physics prescriptions. Variants exploiting resistive compressible MHD setups with guide fields continue to quantify the role of compression versus Ohmic heating in reconnection scenarios, where also the overall (periodic) system size is varied.[9] The Newton challenge type setup has also highlighted, from intercomparing PIC with resistive MHD evolutions, that entropy and mass conservation arguments can be invoked to argue in favor of the validity of MHD descriptions for reconnection scenarios.[10]

However, recent numerical studies performed at higher resolution and/or exploiting more accurate algorithmic approaches gave strong indications that even single fluid resistive MHD may lead to more complex behavior than originally anticipated. This change in viewpoint is already discussed in recent textbooks,[11] where the authors used modern grid-adaptive simulation tools[12] to confirm the original findings on self-feeding turbulent magnetic reconnection by Lapenta.[13] Shortly thereafter, simulations exploring 2D isothermal, compressible MHD convincingly showed[14] the increased reconnection rate for high Lundquist number configurations, through following an extended current sheet forming when four flux

tubes coalesce in an overall double periodic domain. The current understanding hints to the need to exceed a critical Lundquist or magnetic Reynolds number regime (a statement which may need to be augmented with the details of the numerical scheme and overall resolution requirements), in which one can encounter thin enough current sheets, liable to a super-Alfvénic tearing or plasmoid instability. Recent efforts explore ever higher Lundquist number regimes, and have started to provide estimates for the distribution of magnetic flux contained in the plasmoids, using combined analytic and numerical means.[15] At the same time, efforts to explore the fate of these secondary islands in extended physics scenarios, in particular in (reduced) Hall MHD indicate that this intrinsically chaotic regime may show detailed differences between resistive and Hall regimes in the scaling of growth rates and island numbers, when a linear normal mode analysis is performed.[16] In visco-resistive MHD setups, the challenging regime of Lundquist numbers exceeding 10^6 has started to reveal the strongly stochastic nature of the reconnection, with reports of monster plasmoids by consecutive coalescence.[17] Furthermore, high resolution studies[11,18] identified how Sweet-Parker type current sheets subject to plasmoid formation can in turn develop Petschek-like shocks on the inter-plasmoid current layers, making quantitative scaling arguments for these highly nonlinear, time-dependent reconnection regimes extremely difficult.

In this paper, we use a similarly reproducible 2D double periodic setup to the ones used in the GEM and Newton challenges, and vary the overall resistivity (i.e., Lundquist or magnetic Reynolds number) range in combination with performing detailed resolution studies for a range of popularly exploited numerical discretizations. This makes it feasible to discuss the role of secondary island mediated, enhanced reconnection scenarios, and the intrinsic difficulties associated with resolving the detailed chaotic behavior when such instabilities occur. We show how secondary islands can form when exploiting resistivity values of order 0.001, consistent with the original case already showing the islands during the GEM comparison efforts.[19] Here, we complement this with details on the obtained long-term energetic evolutions, where ultimately compressional heating dominates the energy exchange mechanisms. We provide a clear means of quantifying and demonstrating code capability to recognise ideal up to resistive resolving power, and stress the importance of overall conservative treatments to do justice to the nonlinear dynamics. The comparison shows that even at moderate Lundquist numbers compared to those recently reported in the literature, agreement on the precise details and convergence of the solutions is not always guaranteed, although the various simulations can capture the different phases in the dynamics quite well. The paper is organised as follows. In Sec. II, we give all details on the initial condition exploited and the parameter regime selected. In Sec. III, we present simulation results from a modern grid-adaptive finite volume treatment. Then, we discuss in Secs. IV and V the findings obtained by different numerical discretizations targeting the same resistive MHD evolutions, including those originally involved in the GEM and Newton type setups. This allows us to identify trends that are indifferent to the exploited discretization strategies, in a manner which complements the many efforts where different physical realisations are intercompared. A summary and outlook to further work is given in Sec. VI.

II. DOUBLE CURRENT SHEET SETUP

On a 2D square domain $[-15,15]\times[-15,15]$, using double periodic boundary conditions, we wish to study numerically the long-term evolution of a double current layer configuration, subjected to perturbations inducing a tearing-type dominated evolution. Our initial condition is a double GEM-type reconnection problem, and we restrict this study to 2D (visco-)resistive MHD, always adopting a fixed ratio of specific heats $\gamma = 1.666667$ (i.e., 5/3). We take as magnetic field

$$B_x = B_0[-1 + \tanh(y - y_{\rm low}) + \tanh(y_{\rm up} - y)] + \delta B_{x1}\,,$$
$$B_y = \delta B_{y1}\,, \tag{1}$$

where the perturbed field is given by

$$\delta B_{x1} = -\psi_{\rm low}\frac{2\pi}{L_y}\cos\left(\frac{2\pi}{L_x}(x - x_{\rm mid})\right)\left[\sin\left(\frac{2\pi}{L_y}(y - y_{\rm low})\right) + 2(y - y_{\rm low})\cos\left(\frac{2\pi}{L_y}(y - y_{\rm low})\right)\right]$$
$$\times \exp\left(-\frac{2\pi}{L_x}(x - x_{\rm mid})^2 - \frac{2\pi}{L_y}(y - y_{\rm low})^2\right) + \psi_{\rm up}\frac{2\pi}{L_y}\cos\left(\frac{2\pi}{L_x}(x - x_{\rm mid})\right)$$
$$\times \left[\sin\left(\frac{2\pi}{L_y}(y - y_{\rm up})\right) + 2(y - y_{\rm up})\cos\left(\frac{2\pi}{L_y}(y - y_{\rm up})\right)\right]\exp\left(-\frac{2\pi}{L_x}(x - x_{\rm mid})^2 - \frac{2\pi}{L_y}(y - y_{\rm up})^2\right),$$

$$\delta B_{y1} = +\psi_{\rm low}\frac{2\pi}{L_x}\cos\left(\frac{2\pi}{L_y}(y - y_{\rm low})\right)\left[\sin\left(\frac{2\pi}{L_x}(x - x_{\rm mid})\right) + 2(x - x_{\rm mid})\cos\left(\frac{2\pi}{L_x}(x - x_{\rm mid})\right)\right]$$
$$\times \exp\left(-\frac{2\pi}{L_x}(x - x_{\rm mid})^2 - \frac{2\pi}{L_y}(y - y_{\rm low})^2\right) - \psi_{\rm up}\frac{2\pi}{L_x}\cos\left(\frac{2\pi}{L_y}(y - y_{\rm up})\right)$$
$$\times \left[\sin\left(\frac{2\pi}{L_x}(x - x_{\rm mid})\right) + 2(x - x_{\rm mid})\cos\left(\frac{2\pi}{L_x}(x - x_{\rm mid})\right)\right]\exp\left(-\frac{2\pi}{L_x}(x - x_{\rm mid})^2 - \frac{2\pi}{L_y}(y - y_{\rm up})^2\right).$$

We note that this perturbation contains the perturbation amplitudes $\psi_{\rm low}$, $\psi_{\rm up}$, and we will always take them identical on top and bottom layer setting $\psi = \psi_{\rm low} = \psi_{\rm up}$. As discussed further on, the various simulations will vary ψ to cover both unperturbed $\psi = 0$ and deliberately non-linearly perturbed cases where $\psi = 0.1$, a factor 10 lower than the background field amplitude $B_0 = 1$. The geometric parameters are $L_x = 30$, $L_y = 30$ (the domain sizes), and the positions of the current layers are at $y_{\rm up} = 7.5$, $y_{\rm low} = -7.5$ while we identify the horizontal middle as $x_{\rm mid} = 0.0$.

The density profile is taken as

$$\rho = [0.1 + \cosh^{-2}(y - y_{\rm low}) + \cosh^{-2}(y - y_{\rm up})]\,. \quad (2)$$

To get a MHD equilibrium configuration, the pressure profile is set according to

$$p = \frac{B_0^2 \rho}{2}\,. \quad (3)$$

There is no flow at $t = 0$, and we let this system evolve to times $t = 350$. Note that this setup has an initial uniform temperature $T = B_0^2/2 = 0.5$, and a constant internal energy from $e = T/(\gamma - 1)$.

We summarise the most relevant parameters for the different simulations used further on in Table I. Note that we include a resolution study for a pure ideal $\eta = 0$, unperturbed $\psi = 0$ configuration as well, to demonstrate the capability of the numerical approach to maintain a MHD equilibrium over the targeted long-term evolution up to $t = 350$. Our normalisation adopted above implies that our time unit relates to a sound and Alfvén crossing time through the initial current layers. Indeed, the initial $B_x(y)$ profile sets the $t = 0$ current sheet width to order unity, makes the plasma beta exterior to the sheets equal to $\beta = 0.1$, and has a uniform sound speed $c_s = \sqrt{\gamma T} \approx 0.91$ while the Alfvén speed exterior to the sheets is about $v_A = B_0/\sqrt{\rho} \approx 3.16$. The normalization also implies that our dimensionless resistive parameter η relates directly to the inverse prevailing Lundquist number $L_u = 1/\eta$. Note that when we restore the dimensions, the background magnetic field magnitude B_0, the plasma density value in the sheet ρ_0 (our setup has a dimensionless density 0.1 external to the current sheets, and 1.1 as peak density value), and the current layer(s) width l_0 (since our dimensionless profiles have order unity half-widths) combine with permeability constant μ_0 and the plasma resistivity η_0 (the latter, e.g., a Spitzer resistivity expressed in Ohm-meter for SI units) to give $1/\eta = L_u \equiv \frac{\mu_0 l_0 B_0/\sqrt{\rho_0 \mu_0}}{\eta_0}$. Note that the Lundquist number uses the typical Alfvén speed as characteristic velocity, and we used the current sheet width as characteristic length scale l_0. This is important to point out, as different normalizations are abound in the reconnection literature, and quoted Lundquist numbers or magnetic Reynolds numbers (exploiting $R_m \equiv \frac{\mu_0 l_0 v_0}{\eta_0}$ with characteristic speed v_0 and length l_0) may sometimes refer to other choices of typical speeds and lengths, like a sound speed or overall domain size. In our setup, the ratio $c_s/v_A \approx 0.29$ is order unity, making the most important scaling factor the one for the adopted length unit.

TABLE I. The most important parameters for the finite-volume MPI-AMRVAC runs. The leftmost column serves to label the various experiments.

Run	ψ	η	$N_x \times N_y$	Comments
Id1	0	0	240×240	Ideal, no perturbation
Id2			480×480	
Id3			960×960	
Id4			1920×1920	
A1	0.1	0.01	240×240	Resistive, perturbed
A2			480×480	Resistive, perturbed
A3			960×960	Resistive, perturbed
Anp	0	0.01	960×960	Resistive, unperturbed
B1	0.1	0.001	240×240	Resistive, perturbed
B2			480×480	Resistive, perturbed
B3			960×960	Resistive, perturbed
Bnp	0	0.001	960×960	Resistive, unperturbed
C1	0.1	0.0001	240×240	Resistive, perturbed
C2			480×480	Resistive, perturbed
C3			960×960	Resistive, perturbed
C4			1920×1920	Resistive, perturbed
Cnp	0	0.0001	960×960	Resistive, unperturbed

III. FINITE VOLUME BASED SIMULATIONS

In this section, we will first concentrate on the observed trends within the set of simulations from Table I as performed with a modern grid-adaptive, finite volume based code, MPI-AMRVAC.[12] The resolutions mentioned will thereby relate to *effective* resolutions, corresponding to the highest grid level allowed in the adaptive block-quadtree mesh. We always enforce the highest resolution throughout both current layers, and further use automated regridding based on a weighted second derivative expression for density and both magnetic field components in the rest of the domain. The resolution studies are then actually achieved by allowing more levels on top of an overall fixed base resolution of 60×60. The discretization combines a three-step Runge-Kutta explicit temporal scheme with a TVD Lax-Friedrichs discretization where the spatial reconstruction employs the recent third order Čada limiter.[20] This combination of spatio-temporal discretizations realises third order accuracy on smooth solutions, is shock-capturing, and fully conservative.

A. Resolving ideal to resistive long-term behavior

The results of the ideal MHD resolution study from MPI-AMRVAC are shown in Fig. 1. The figure shows three means of demonstrating that the numerical discretization at hand is capable of maintaining a MHD equilibrium over many dynamical timescales. The top panel shows the energy balance, and this global quantifier of the evolution is in essence identical for all resolutions employed. We show as a function of time total, magnetic and internal energy given by

$$E_{\rm Total} = \frac{1}{V}\int\int\left(\frac{p}{\gamma - 1} + \frac{B^2}{2} + \frac{\rho v^2}{2}\right) dx\, dy\,, \quad (4)$$

$$E_{\rm Magnetic} = \frac{1}{V}\int\int\left(\frac{B^2}{2}\right) dx\, dy\,, \quad (5)$$

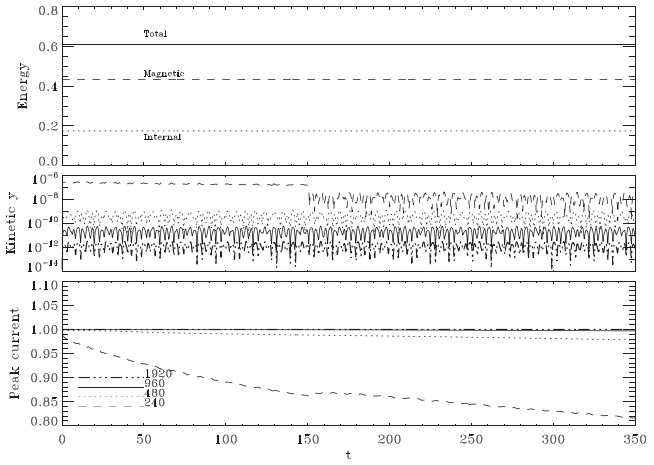

FIG. 1. Demonstrating the convergence behavior for an ideal MHD equilibrium using a finite volume, grid-adaptive code. Top panel: the conservation of total energy over long timescales, and its constant division over magnetic and internal energy, primarily. Middle panel: the remnant kinetic energy associated with small-scale waves running vertically through the periodic domain is fully negligible, and near-vanishes for increasing effective resolution (from 240^2 to 1920^2). Bottom panel: The instantaneous maximal value of the current is the most stringent test for qualifying numerical diffusion in convergence tests, and from 480^2 onwards is as good as constant up to $t=350$.

$$E_{\text{Internal}} = \frac{1}{V}\int\int\left(\frac{p}{\gamma-1}\right)dx\,dy\,, \tag{6}$$

where we integrate over the full domain $V = L_x L_y$. The total energy is conserved perfectly, due to the conservative nature of the numerical scheme, and the division over magnetic to internal energy is seen to be kept constant during the entire simulation. Note that although we ran the configuration in 2D, the ideal unperturbed setup maintains a 1D nature throughout. The second panel quantifies the effects of increasing the resolution by showing similarly the kinetic energy as a function of time. This remains negligibly small for all resolutions employed, dropping from $\mathcal{O}(10^{-7})$ down to $\mathcal{O}(10^{-12})$ by increasing effective resolution from 240^2 to 1920^2. The individual fluctuations relate to small-amplitude wave features running vertically through the domain (only y-components develop). This global measure of the deviation from a true static ideal MHD equilibrium can safely be related to remaining artificial dissipation, which is otherwise inherently difficult to quantify due to the nonlinearities involved in the reconstruction procedures used in shock-capturing finite volume approaches. The test shows that even at 240^2, an acceptably low numerical dissipation is present. The final, most stringent quantification shown for all resolutions used is the maximal current value throughout the domain, which is at all times found in both current layers. The initial $t=0$ value differs from 0.991 at 240^2 to 0.99986 at 1920^2, as the resolution through the initial current sheet varies. This local quantifier of the numerical dissipation shows that the 240^2 resolution gradually diffuses the equilibrium (with an adjustment at about $t=150$) such that the current peak value diminishes. However, from resolutions 480^2 and above, the peak current adjustment is virtually absent, and the remnant dissipation as a result of (accumulated) truncation errors can be fully ignored: peak current values at $t=350$ are still 0.99983 for the highest resolution.

A second resolution study, shown in Fig. 2, quantifies similar global and local measures for a resistive MHD run at resistivity $\eta=0.01$. This high resistivity value effectively ensures that the evolution of the double current layer system is entirely controlled by the ongoing Ohmic dissipation. In fact, Fig. 2 demonstrates that in this magnetic Reynolds regime, the system behaves almost identical between perturbed (A1, A2, and A3) versus unperturbed (Anp) cases. The energetic evolution is quantified in the lower two panels, and shows that while total energy is conserved (still exactly true for resistive MHD simulations), the evolution up to $t=350$ gradually exchanges magnetic for internal energy. This exchange happens directly through Ohmic heating, quantified in the lower right panel from

$$H_{\text{Ohmic}} = \frac{1}{V}\int\int \eta J^2\,dx\,dy\,. \tag{7}$$

The integral under this curve correlates exactly with the change in internal energy, at the expense of magnetic energy through resistive diffusion. While the lower panels give the same global quantification of this effect for unperturbed versus perturbed cases, the top panels show how local (peak current) and global (kinetic energy in the y-direction) measures show some detailed differences. The peak current for the unperturbed case, shown as a dashed-dotted line, decreases gradually, this time entirely resulting from the ongoing Ohmic dissipation. The three different resolutions used for the perturbed case show that despite the initial non-linear perturbation in the magnetic field, the system does not transit to a sustained reconnection regime, but rather evolves to the trend already present for unperturbed (and in fact pure 1D) evolution. The resolution is also sufficient to claim fully converged evolutions, as all three cases (A1, A2, A3) agree on the peak current values, and show the same global kinetic energy measure, with only the 240^2 case slightly overshooting in maximal value (top right panel) while the curves for 480^2 and 960^2 overlap completely.

B. Secondary islands in chaotic phases

While the cases discussed thus far show well-known behavior in ideal to resistive settings, we now discuss the simulations exploring higher Reynolds number regimes. By lowering the resistivity to $\eta=0.001$, i.e., one order of magnitude with respect to the previous cases A, the perturbation in the initial magnetic field is now capable of enforcing a transit to a tearing-type reconnection regime, previously studied extensively in the GEM-challenge setups. When we follow the evolution up to long-term, we find distinct phases in its overall energy budget, as quantified in Fig. 3, top panel. This panel combines the energetic evolutions for both unperturbed case Bnp (as dashed-dotted lines, almost staying horizontal), as well as for perturbed case B3 at the highest employed resolution. Obviously, the total energy remains conserved for each case, but while the unperturbed case now only shows a minor exchange from magnetic to internal

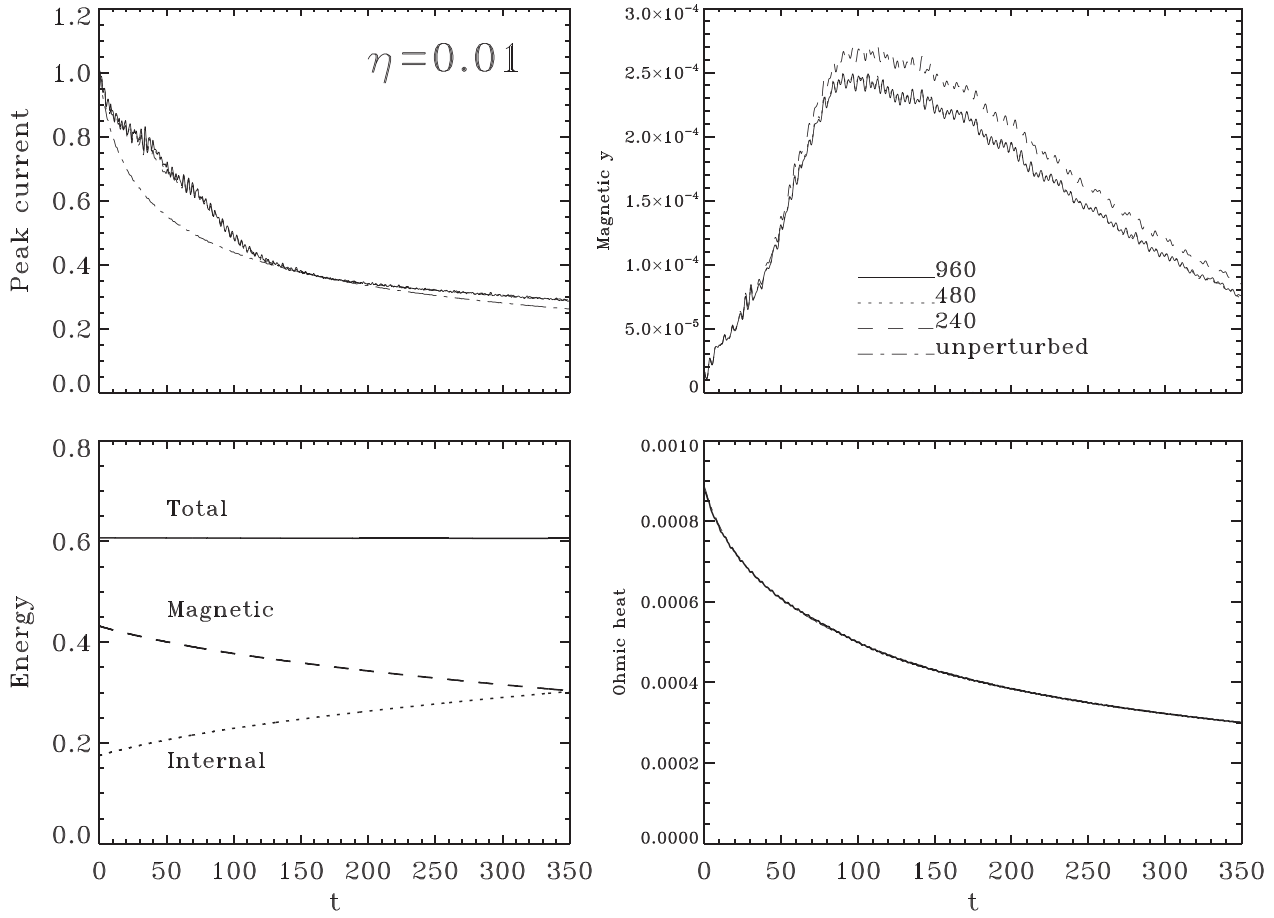

FIG. 2. The temporal evolution for a resistive MHD case with $\eta = 0.01$. Top left panel: The dashed-dotted line shows the peak current value evolution when no perturbation is imposed, an evolution purely due to Ohmic diffusion. The other three lines (which are near-indistinguishable) show the same for a perturbed case, for 240^2 till 960^2, showing excellent convergence. Top right panel: The same four cases are quantified in terms of their evolution in magnetic energy in the y-component. The dashed-dotted line remains zero throughout, the other three demonstrate clear convergence (solid and dotted fully overlap). Bottom left: the evolution of total energy, which is conserved in resistive MHD, and the exchange of magnetic to internal energy due to Ohmic heating (this plot is identical for all 4 cases). Bottom right: the evolution of the Ohmic heating as function of time (also near-identical for all 4 cases).

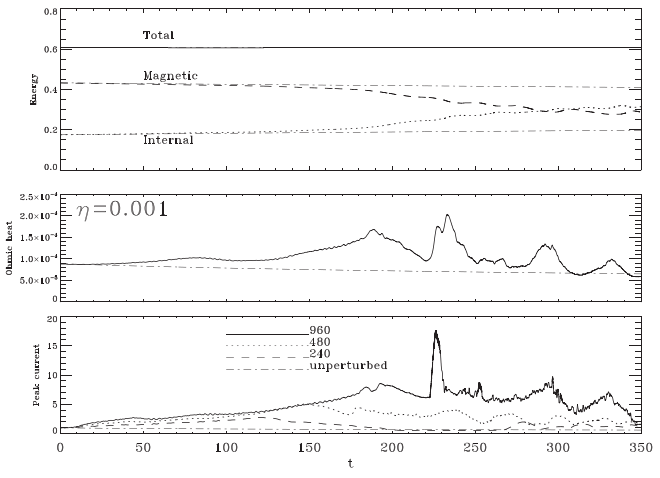

FIG. 3. At $\eta = 0.001$, clear differences in energetic behavior occur between an unperturbed and perturbed scenario. Top panel: Total energy staying constant for both, the exchange of magnetic and thermal energy deviates strongly from pure Ohmic-mediated evolutions beyond $t \approx 150$. Dashed-dotted lines are for unperturbed case, the dashed (magnetic) and dotted (internal) for the 960^2 simulation B3. Middle panel: comparison of Ohmic heating evolution for unperturbed (dashed-dotted line, Bnp) to perturbed (solid, B3) case. Bottom: the peak current evolution for cases Bnp, B1, B2, B3 from Table I as function of time.

energy over the full $t \in [350]$, a dramatic change is seen for the perturbed case from roughly $t \approx 150$ onwards. The minor change from magnetic to thermal energy in the unperturbed case is once more fully explained by Ohmic heating, quantified in the next panel for both case Bnp and case B3. We then observe that although the perturbed scenario shows somewhat larger Ohmic heating throughout, its order of magnitude cannot explain the dramatic change witnessed in magnetic to internal energy seen for the perturbed case B3. In fact, the changeover at about $t \approx 150$ in this latter case coincides with a significant rise in the peak current value obtained in the centre of both current-sheets. This latter rise in instantaneous maximal current value is plotted for all four cases B1, B2, B3, and Bnp in the lower panel of Fig. 3. From this local quantifier of numerical "convergence," it is seen how resolutions 480^2 and higher agree up to this time in their overall evolution. Indeed, up until this time, the system looks virtually indistinguishable as seen in current maps for the three cases B3 (left), B2 (middle), and lowest resolution B1 (right) at time $t = 100$, shown in Fig. 4. They demonstrate the archetypal evolution with a centrally collapsed, narrow current sheet connecting a continuously growing magnetic island structure found across the periodic side boundaries.

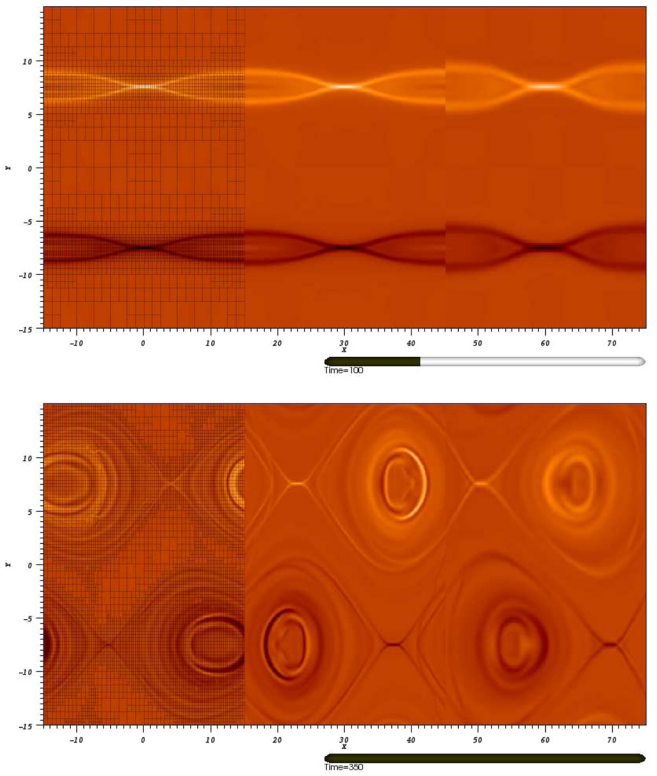

FIG. 4. Instantaneous snaphots of the current distribution at times 100 (top) and $t = 350$ (bottom) from the simulations B3 (left), B2 (middle), and B1 (right), i.e., from high to low resolution. The color scale is taken identical in range between all three panels. At far left, the adaptive grid structure is superimposed, each square represents a grid block of size 10×10. Note how qualitatively speaking, both the initial phase and the final endstate share many features in common.

During this phase, which has been studied extensively in the literature, a gradual transfer of magnetic flux into the island structure happens, fully mediated by the local dissipative region at the centres of both layers. Figure 4 also shows the instantaneous grid structure used in the highest resolution case B3. The difference in current structure at $t = 100$ confirms visually the role of numerical diffusion still present at 240^2 (B1 at right), as the side island structure is seen to be wider than in the other panels. The peak current evolution collected in Fig. 3 demonstrates deviations between the higher resolution cases from about $t \approx 150$, and these signal the spontaneous appearance of secondary islands through the centrally collapsed current sheet regions. For case B2, such secondary island structures already appear at about $t \approx 150$, while at higher resolution (B3), they form at about $t \approx 190$. At the highest resolution, these secondary islands tear up the central current sheets (see also Fig. 8, top panel for a similar view on case C), consecutively grow to macroscopic dimension, and ultimately break the left-right symmetry, in this case by merging with the large island structures to their right. A vertical cut (at $x = 0$, $t = 197$ for run B3) through these secondary islands is shown in Fig. 5, and one clearly recognises the typical tearing eigenfunction behavior of the temperature and transverse magnetic field perturbations. Their subsequent merging with the larger island structures is marked by pronounced peak current variations, seen at about $t \approx 225$ in Fig. 3, bottom panel. Both the 480^2 and 960^2

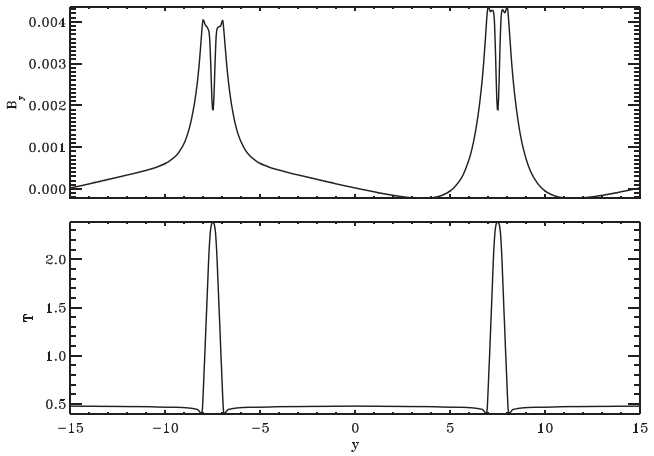

FIG. 5. A cut at $x = 0$ through the middle of the domain, for run B3 at $t = 197$ shows how the detailed variation of the $B_y(y)$ and temperature $T(y)$ clearly contain the tearing mode eigenfunction variations through both top and bottom current sheets. At this point in the evolution, both current layers show a clear secondary island developing, much like in Figure 8, top panels.

simulations demonstrate this transit to a chaotic phase with eventually multiple smaller islands forming and merging erratically with the largest island structure. This phase correlates well with the effective magnetic to internal energy transformation seen in the top panel of Figure 3. The reconnection and flux reshuffling then progresses much faster, leading to truly enlarged island structures which interact by compressive means. Indeed, the top and bottom islands finally enter cycles of left-right, up-down asymmetric movements. By considering the full energetic balance, this chaotic phase also has significant velocities in parts of the domain, which are the main reason why the internal energy becomes much more enhanced above the corresponding unperturbed scenario Bnp. Although the energetic evolutions show similar trends when increasing resolutions from B1 to B3, there is no possibility for achieving "strong convergence" (i.e., exact agreement by increasing the resolution), as even the slightest change in numerical treatment (discretization, truncation error) induces variations in the details of this longer term chaotic phase. However, the resolutions adopted are sufficient to capture the final long-term fate of the double current sheet system. This statement is made visual in the bottom panel of Fig. 4, showing the current structure at $t = 350$ for B1 to B3. There, we see how ultimately the islands have reached vertical extents beyond half the domain size, resulting in top and bottom current layers interacting compressively. Note that the detailed current structure throughout the islands shows clear evidence of the multiple island mergers which have already happened by then, and how the fine-structure increases from B1 to B3, in line with the chaotic phase behavior discussed.

C. High magnetic Reynolds number scenarios

By lowering the resistivity another order of magnitude, setting the assumed uniform $\eta = 0.0001$, the transition to the chaotic phase with secondary tearing events enhancing the overall reconnection raises the demands for resolving this complex long-term behavior. Still, from about resolutions of

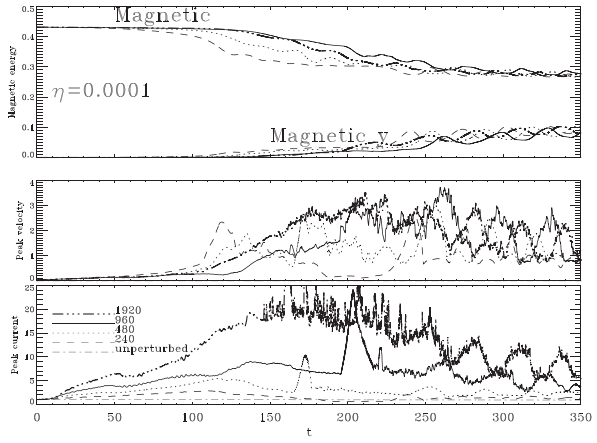

FIG. 6. For $\eta = 0.0001$, resolution study and comparison with the unperturbed scenario for cases C1, C2, C3, C4, and Cnp. Top panel: the magnetic energy evolution for the four perturbed cases, as well as the contribution of the *y*-component of the magnetic field to this quantity. Middle panel: the peak velocity as function of time for cases C1 through C4. Bottom panel: the peak current, for unperturbed as well as perturbed cases C1 to C4.

480^2 and higher we find overall agreement in the trends observed, as summarised in Fig. 6. Its top panel quantifies the magnetic energy evolution, showing both the total magnetic energy, as well as the magnetic energy in the transverse component alone, for all runs C1, C2, C3, and C4. The solid line corresponds to the reference 960^2 resolution used in case C3, and after time $t \approx 130$ the decrease in overall magnetic energy content signals the corresponding increase in thermal energy, which in the later evolution is significantly influenced by adiabatic compression events. The resulting growth of the original island structure by merging events from secondary islands also renders the fractional energy stored in the transverse field significant. The presence of strong compressive events is quantified in the second panel of Fig. 6, which shows the instantaneous maximal velocity for all runs C1 to C4. These peak velocities are seen to reach values well above the initial sound speed and up to the Alfvénic speed. The lower panel shows the corresponding peak current value for all cases, also showing the unperturbed run Cnp which perfectly maintains the current sheet structure as explained earlier. This peak current, as a stringent local measure for "convergence" still increases when further doubling the resolution in each direction, while the energetic behavior allows to draw the same conclusions as in case C3. To give a better impression of the dynamics as a function of time, Fig. 7 shows the current structure (actually employing the logarithm of its absolute value) through both bottom (left) and top (right) current sheets as a function of time. In this view, one can recognise at all times the largest periodic side island (labelled "A"), and at time $t \approx 130$ the appearance of the central secondary island tearing the current layers (labelled "B"). For this run C3, the left right and up-down symmetry is perfect up to about $t \approx 150$, and then symmetry-breaking occurs, with in this case the central islands ultimately both merging with the large island to the left (labelled as "C," this coincides with the sudden peak current evolution seen in Fig. 6, lowest panel). The central current sheets are always corresponding to the central lighter shaded regions, and the chaotic islands appearing and merging with the large island are visible in this view as small striations (labelled as "D"). One can see also the overall left-right displacements of the larger side island in the phase labelled as "E," which correspond well to the variations in energy exchange seen in the previous plots (like in Fig. 6, top panel). Snapshots of the

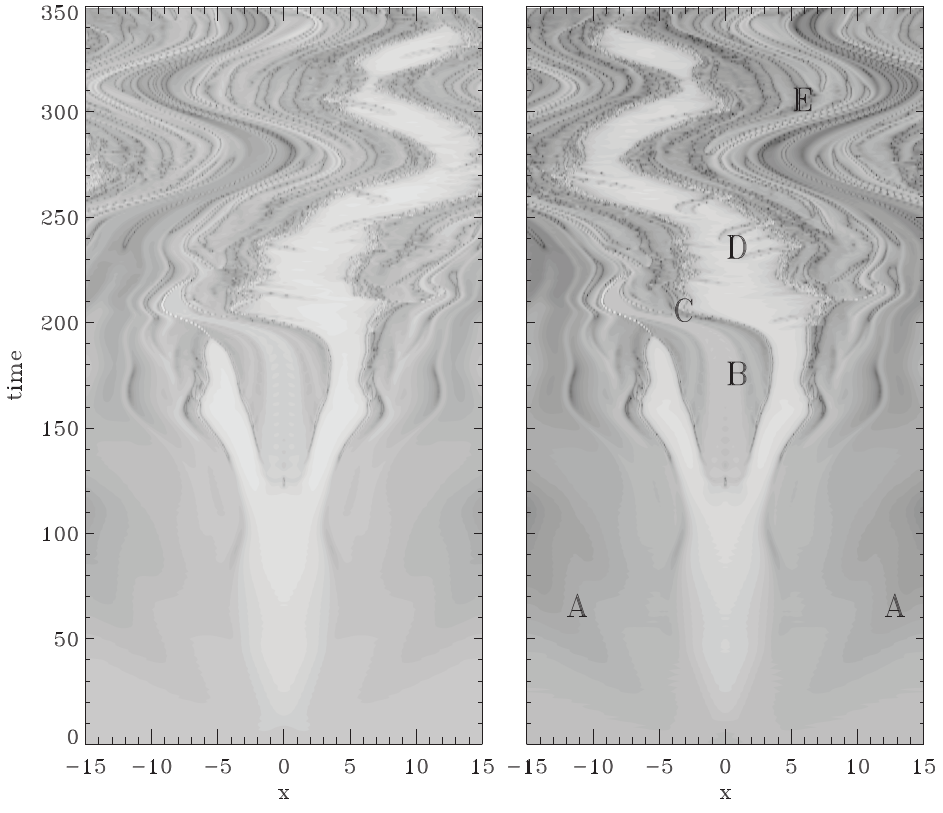

FIG. 7. For case C3 (960^2 for $\eta = 0.0001$, perturbed), we show the current evolution across the middle of both current sheets (at $y = -7.5$ at left, at $y = 7.5$ at right) as function of time. We plot the logarithm of the absolute value of the current. On the right panel, specific features are discussed in the text as labeled, such as the central island forming (B), and the smaller chaotic island dynamics (D).

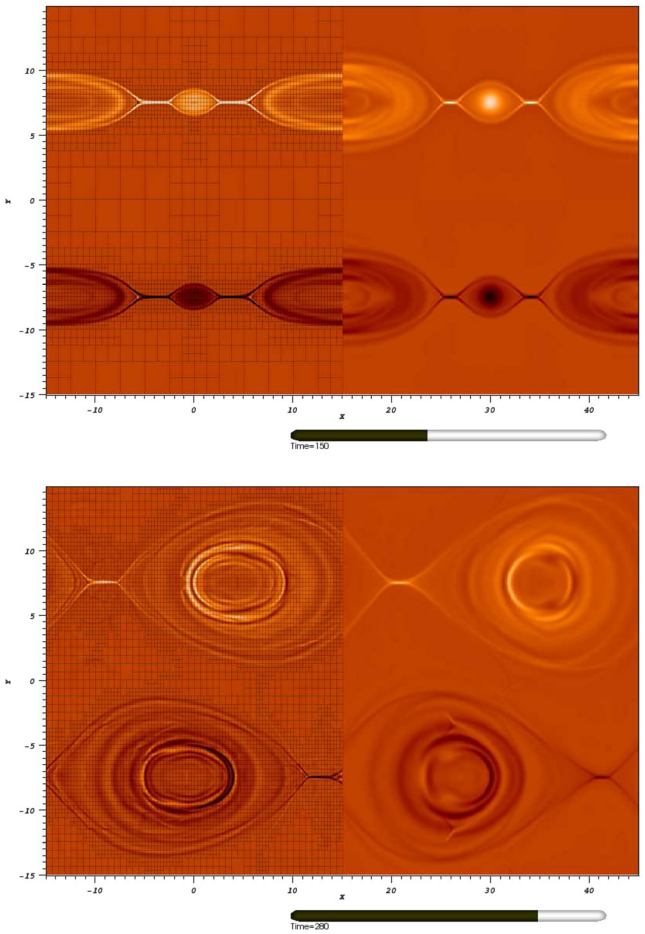

FIG. 8. Instantaneous snaphots of the current distribution at times 150 (top) and $t = 280$ (bottom) from the simulations C3 (left) versus C2 (right), i.e., from high to low resolution. The color scale is taken identical in range between both panels. At far left, the adaptive grid structure is superimposed. Qualitatively speaking, both the phase demonstrating the central island growth, and the final endstate, agree.

current distribution from cases C2 and C3 at selected times $t = 150$, 280 are given in Figure 8, which demonstrate in a manner similar to Fig. 4 how qualitative agreement is obvious among resolution-enhanced runs, albeit differing details relating to the chaotic behaviour and the fine-scale structuring of the islands show the clear need for extreme resolution studies. Run C4, at 1920^2 resolution, demonstrates this well, and some representative snapshots are shown in Fig. 9. At these resolutions, it becomes possible to (i) identify how secondary island mergers induce shock wave fronts propagating through the regions exterior to the large islands; (ii) to identify details in the wave patterns resulting from the multiple coalescence events within the merged island structures, and (iii) to start making statements on turbulent aspects in both thermodynamic and magnetic field quantities. Figure 9 does so visually, by plotting both the current distribution next to a Schlieren plot of the density field, i.e., a logarithmically stretched view on the density gradients. This allows to identify clearly shock fronts (as the merging events involve up to superAlfvénic speeds, as discussed above), and the various magneto-acoustic signals traversing the domain.

The most stringent measures of "resolving" the chaotic, long-term trends are thereby invariably the quantifications of peak current and velocity, and we collected their evolutions for cases Id2, A2, B2, and C2 all at 480^2 resolution in the left panels of Fig. 10, while the same info for the 960^2 runs Id3, A3, B3, and C3 are shown in the right hand side panels. This plot thereby confirms that the resistivity has to be sufficiently low (or equivalently, the magnetic Reynolds regime must exceed a critical value) in order to enter the ultimate chaotic regime. At the same time, these local quantifiers of the complex dynamics agree only qualitatively when increasing the resolution. At the same time, we can see a clear correlation for increasing peak currents realised at lower resistivities, a trend for interrelated peak current-peak velocity measures, and an overall agreement in the cyclic behavior due to the large-scale side island movements (seen as "E" in Fig. 7) and their resulting energetic evolutions.

IV. FINITE DIFFERENCE RUNS WITH THE COPENHAGEN STAGGER CODE

The Copenhagen stagger code[21–23] represents a high order finite difference code, a variant of which was involved with the mentioned Newton challenge. For this work, we use a uniform grid resolution. The code uses staggered grids combined with high order operators to provide the interpolation and differentiation between the staggered grids. It normally employs a 6 gridpoint wide stencil to provide a 6th order accurate first order functional derivative and a 5th order accurate grid interpolation. In standard applications, simulations use a dedicated approach to impose diffusion and resistivity only in locations where numerical problems from the stagger operations and physical conditions can be predicted to arise. This implies that typically four parameters are used to control the diffusivity. These react in relation to locations of compression (shocks), steep gradients in the background profiles as in the advection of a top-hat function, and similar situations for the magnetic field. The reason for using this approach in the code arises from the high order methods tendency for producing ringing around strong gradients. To smoothly handle a shock front, one therefore has a number of gridpoints comparable to the stencil size across it. Discontinuities will appear wider in this code than for a low order or Riemann solver based code. The solution is advanced in time adopting a 3rd order Runge-Kutta approach, i.e., similar to the finite volume code used above. For the specific study done here, a rewrite of the diffusion handling has been implemented to also allow the finite difference code to use a constant value for both viscosity and resistivity. We will comment on both this, non-standard, approach for finite difference runs, as well as mention experiments using different stencil widths (2, 4, and 6 point stencils have been employed in the cases where constant diffusion parameters were used). As an important difference to the MPI-AMRVAC code, the prime variables in the adopted MHD equations are density, momentum, thermal energy and magnetic field. The usage of the thermal energy in the energy equation implies that a conservation of total energy is not imposed in the code. The reason for not solving for the total energy was because the main interest of past research with this code concentrated on the low beta plasma of the solar

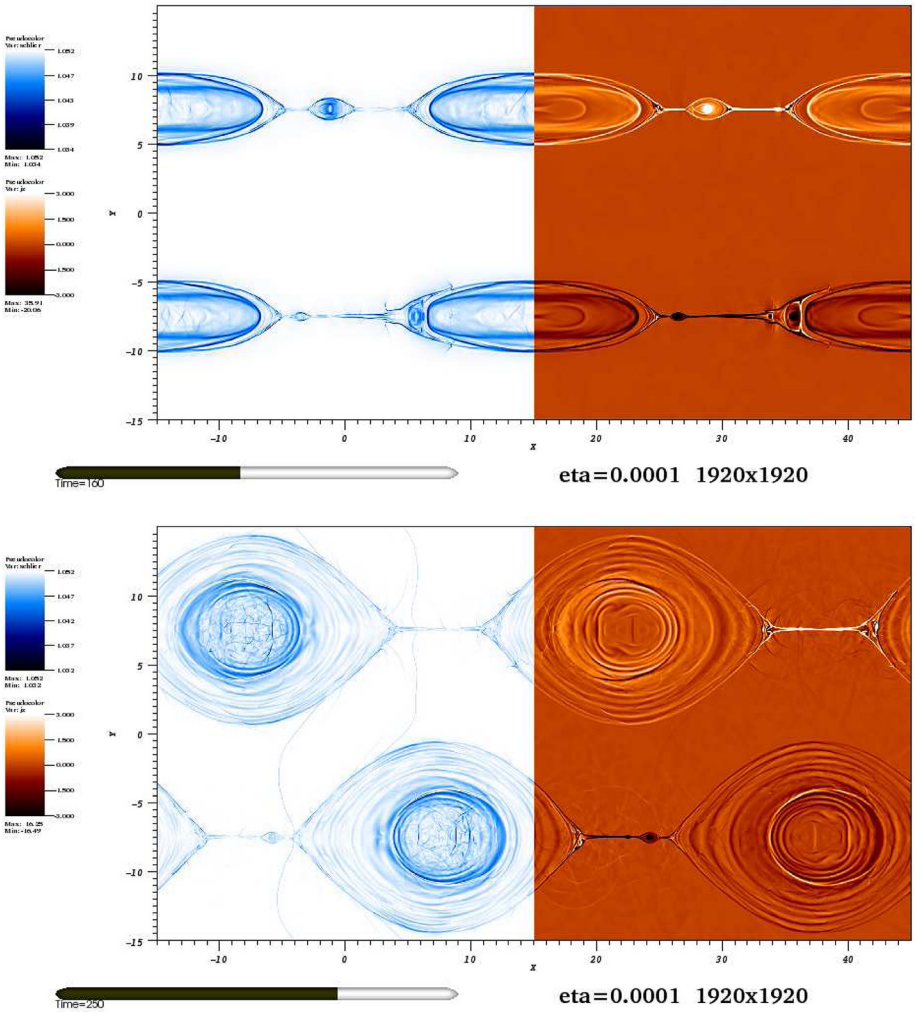

FIG. 9. Two snapshots of the highest resolution run C4 with MPI-AMRVAC. Top panel at $t = 160$, bottom at $t = 250$. Left frames show a Schlieren plot of the density distribution, showing the secondary islands, the shock features induced by coalescence events, and the many wave features criss-crossing the growing island structure. Right frames show current distributions.

corona. Using the total energy would in this case give rise to large possible errors in deriving the plasma pressure and from this the determined temperature. Also, the non-ideal runs always use visco-resistive prescriptions, while MPI-AMRVAC runs did not employ any explicit viscosity terms.

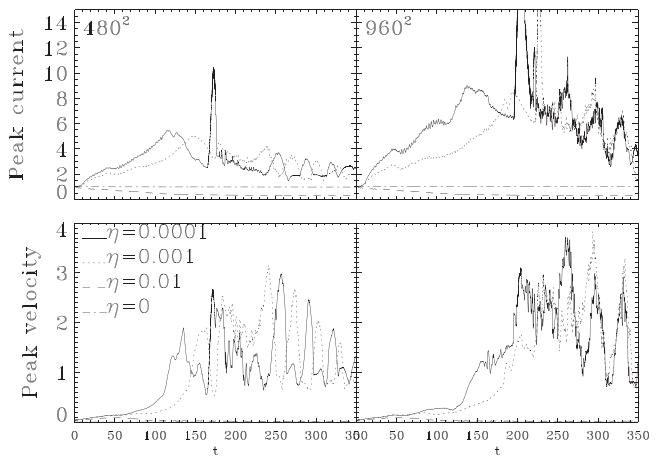

FIG. 10. Overview of all runs with the finite volume approach at 460^2 (left) versus 960^2 (right) intercompared in terms of the two most stringent "convergence" quantifiers: the peak current (top), and the peak velocity (bottom). Clear trends with resistivity parameters are evident, a critical value lies in between $\eta = 0.01$ and $\eta = 0.001$ cases.

A. Unperturbed experiments

To show how a finite difference code handles the initial unperturbed setup, this experiment is repeated here with a uniform grid with resolutions covering 480^2, 960^2, and 1920^2 grid points. We find, similar to the finite volume result from Fig. 1 that the code maintains the equilibrium, and the thermal energy has rms variations on the order of $\mathcal{O}(10^{-6})$ to $\mathcal{O}(10^{-7})$ for the different resolutions. Here it has to be mentioned that the code by default uses 4 bit numbers, or single precision, in comparison to 8 bit numbers, double precision, for the MPI-AMRVAC code. The numbers above are therefore on truncation levels and the result is comparable to the finite volume result. Similarly, the variations in the magnetic energy are in the order $\mathcal{O}(10^{-7})$ for all resolutions, and the kinetic energy $\mathcal{O}(10^{-12})$. This shows that the initial ideal MHD setup is well resolved and stable for all used numerical resolutions when assuming zero viscosity and resistivity.

For a further comparison, the same unperturbed setup has been conducted using a constant numerical resolution 960^2, while the constant value of the viscosity and resistivity was changed from 0.01 to 0.0001 as shown in Table II. Run CS-Anp with $\eta = \nu = 0.01$ has a finite volume analogue with run Anp from Table I and Fig. 2, and CS-Bnp corresponds to run Bnp from Fig. 3, while CS-Cnp is like run Cnp from Table I. Figure 11 shows three sets of lines, the top ones (all

TABLE II. The runs performed with the finite difference Copenhagen Stagger code.

Run	ψ	η	$N_x \times N_y$	Comments
CS-Id2	0	0	480×480	Ideal, no perturbation
CS-Id3	0	0	960×960	
CS-Id4	0	0	1920×1920	
CS-Anp	0	0.01	960×960	Resistive, no perturbation
CS-Bnp	0	0.001	960×960	
CS-Cnp	0	0.0001	960×960	
CS-A2	0.1	0.01	480×480	Resistive, perturbation
CS-A3	0.1	0.01	960×960	
CS-A4	0.1	0.01	1920×1920	
CS-B2	0.1	0.001	480×480	Resistive, perturbation
CS-B3	0.1	0.001	960×960	
CS-B4	0.1	0.001	1920×1920	
CS-B3a	0.1	0.001	960×960	Resistive, perturbation, second order
CS-B3b	0.1	0.001	960×960	Resistive, perturbation, fourth order
CS-C2	0.1	0.0001	480×480	Resistive, perturbation
CS-C3	0.1	0.0001	960×960	
CS-C4	0.1	0.0001	1920×1920	
CS-N2	0.1		480×480	Numerical resistive, perturbation
CS-N3	0.1		960×960	
CS-N4	0.1		1920×1920	
CS-N5	0.1		3840×3840	

overlapping) represent the total energy as defined in Eq. (4) for the different experiments as a function of time. The middle curves represents the magnetic energy, Eq. (5), evolution, and the bottom ones the thermal energy, Eq. (6). Here the different dashed type lines represent the different cases including resistivity. From the top line it is seen that even with this different handling of the energy equation, the total energy is well conserved in the system, while the amount of diffusion depends on the imposed diffusion values.

B. Constant resistivity finite difference experiments

Experiments with constant and equal values of the resistivity and viscosity have been conducted for a series of different numerical resolutions and stencil orders, in order to make direct comparisons with the other codes. As pointed

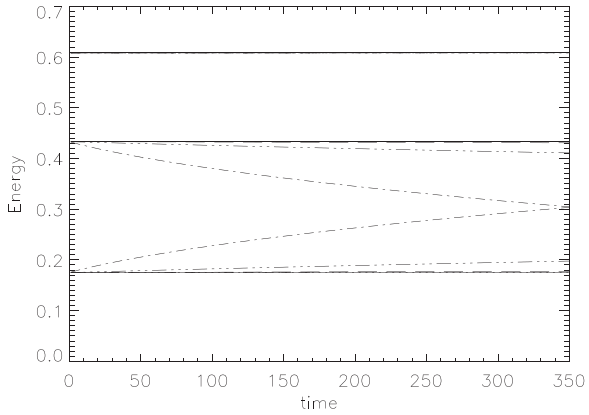

FIG. 11. Energy graphs for the finite difference runs with zero perturbation at 960^2, ideal to visco-resistive. The three sets of lines represent the (top) total energy, (middle) the magnetic energy and (bottom) the thermal energy. The full line is for zero resistivity and demonstrates stable equilibrium. The dashed-dotted lines, dashed-triple-dotted lines, and long dashed lines represent η values 0.01, 0.001, and 0.0001, respectively.

out above, this is not the standard setup for the stagger code, and as a result the code is not always able to handle experiments with low constant diffusive values. The reason in all cases arises from overshooting (reaching negative values) of the thermal energy in the region around the developing strong current sheets. It is to be emphasised that using uniform diffusion parameters is a-typical, as finite difference approaches usually (need to) apply some hyperdiffusion approach, which will also be demonstrated further on. Constant diffusion experiments have been conducted using $\eta = \nu = 0.01,\ 0.001$ and 0.0001. Only for the largest η value did all experiments reach $t = 350$, while for the lower values, experiments stopped earlier, depending on numerical resolution and stencil width. In the following we briefly discuss these different experiments.

1. $\eta = \nu = 0.01$ experiments

For $\eta = \nu = 0.01$ the time evolution of the energy is shown in Fig. 12, which is to be contrasted with Fig. 2 from the finite volume runs.

Figure 12, left panel, shows that the total energy conservation is good for this case. Differences in behavior is seen in

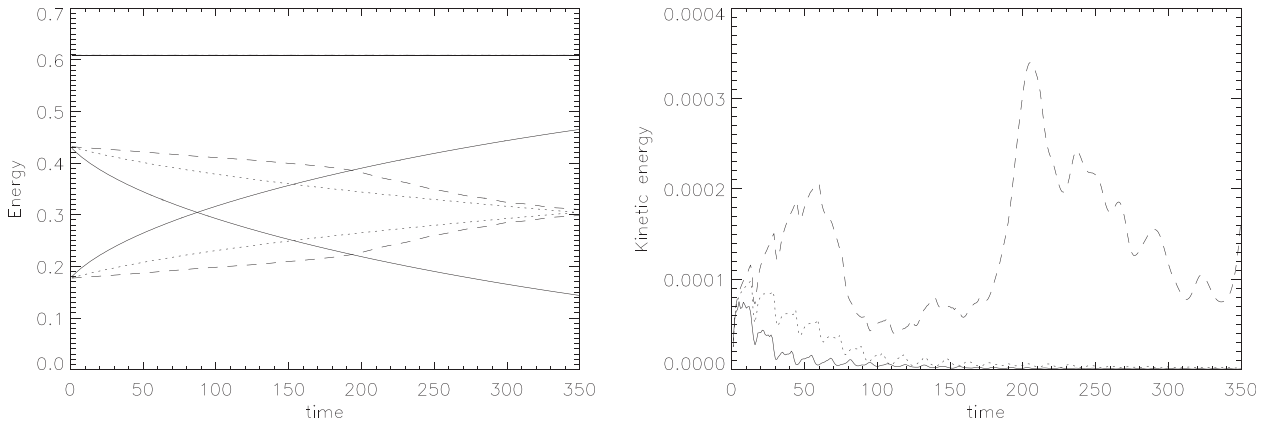

FIG. 12. Left: Energy graphs for the perturbed runs with $\eta = 0.01$ for different numerical resolution. The lines represent: 480^2 full line, 960^2 dotted line, and 1920^2 dashed line. Right: Kinetic energy for the same runs.

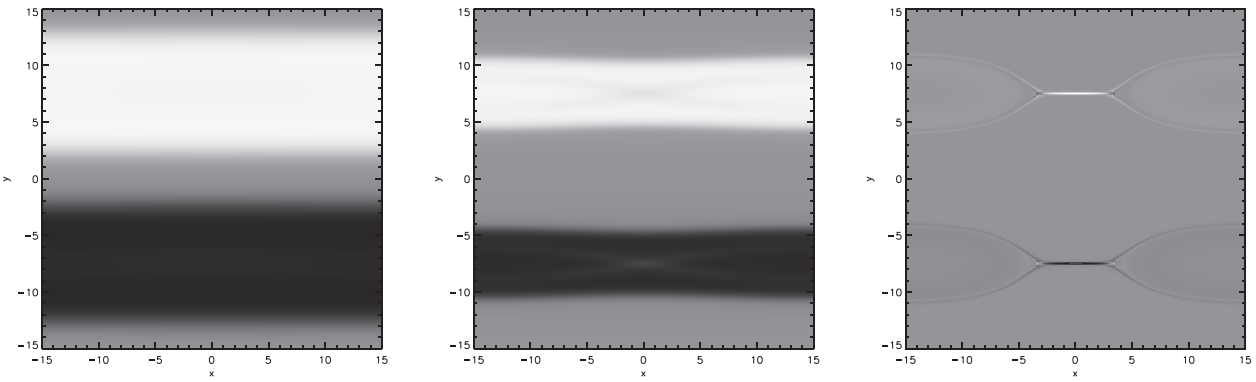

FIG. 13. The three panels show the electric current for the three finite difference experiments with imposed constant $\eta = 0.01$ at $t = 250$. From left to right: 480^2, 960^2, and 1920^2 gridpoints.

the thermal and magnetic energy between the different resolution runs, with the low resolution run clearly deviating as the diffusion of the magnetic energy is much larger than for the two higher resolution experiments. These on the other hand seem to converge towards the same final solution at $t = 350$. Comparing with the MPI-AMRVAC results, it seems the stagger code requires a higher numerical resolution to approach convergence in the result using a constant diffusion approach. Figure 12, right panel, shows the development of kinetic energy for the three experiments. This clearly shows a different behaviour of the high resolution experiment. For the two low resolution runs, the diffusivity is so large that the imposed stress is not able to set up a strong localised current sheet and only a slow diffusion happens without forming concentrated current sheets through which faster magnetic reconnection can proceed. In contrast to this, the high resolution experiment forms a thin current sheet and the following dynamical evolution starts differing significantly between the experiments for the remaining time. The difference in the structure of the electric current profile for the three experiments is shown in Fig. 13 for $t = 250$. Hence, numerical resolution is important for the evolution, and too low resolution imposes too much diffusion, preventing the current sheets to form.

2. $\eta = \nu = 0.001$ experiments

Repeating the constant diffusion parameters, finite difference experiments, with $\eta = \nu = 0.001$ (the CS-B* series) shows that the differences in the evolution between the numerical resolutions vanish, and allow the structure in all cases to transit to a state containing strong central current sheets. Five runs are performed, with varying stencil widths and resolutions, but not all manage to reach $t = 350$. Only within the final 50 time units do clear differences in the energy quantities show up. The three runs with the high order stencil show very comparable development in the energy quantities for the duration they manage to run. The two experiments clearly deviating are those with a decreased stencil width in the stagger operators. Looking at the physical parameters of the three equivalent resolution experiments, a clear difference in this phase of the experiment is observed. In all cases, strong central current sheets develop before $t = 200$ and the physical values are comparable. After this time the current sheets become tearing unstable and a series of plasmoids are formed in all experiments. The difference between experiments encompasses the fact that the plasmoid sizes may differ radically. This may be seen in Fig. 14 showing the electric current for the three different stencil runs with 960^2 resolution at $t = 255$ (from runs CS-B3, CS-B3a, CS-B3b). An inverse size dependence of the plasmoids with the stencil size is noticed, providing the largest and most stable plasmoids for the experiment with the lowest stencil width. The dynamics of these plasmoids are seen at late times in the energy plots (not shown).

3. $\eta = \nu = 0.0001$ experiments

For the lowest $\eta = \nu = 0.0001$ value (CS-C* series), the constant visco-resistive experiments all cease much earlier

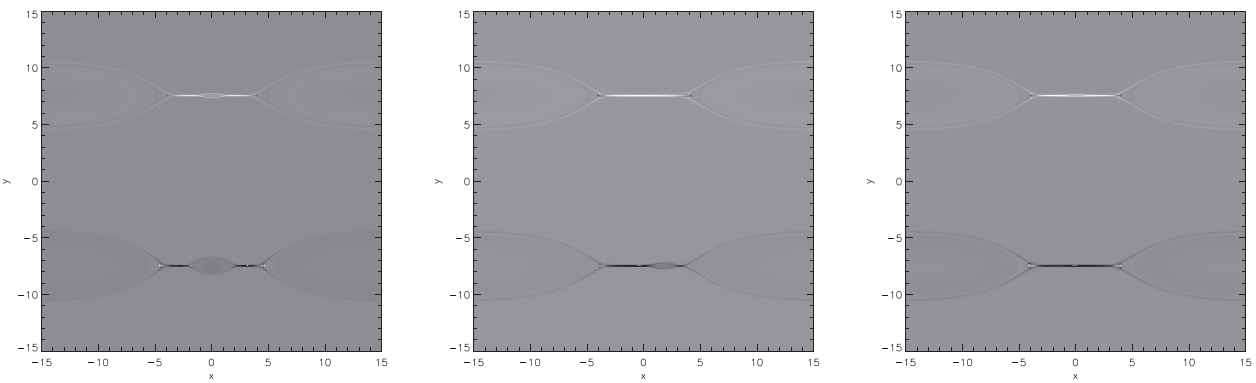

FIG. 14. The three panels show the electric current for the three finite difference experiments with imposed constant $\eta = 0.001$ at $t = 255$ using different stencil widths at fixed 960^2 resolution. From left to right: 6, 4, and 2 point stencil widths.

than the dynamically active phase. The finite difference code is not sufficiently diffusive to smooth out the large gradients that arise in the experiment and locally negative values of the thermal energy occur due to overshooting in the operators moving information between the staggered grids. When monitoring kinetic energy it is seen how all experiments reach a given time, and then this energy starts growing exponentially, leading to code collapse.

4. Global evolution comments

For the MPI-AMRVAC experiments, it was noticed that after a time of reconnection and general growth of the two large plasma blobs, the large scale magnetic field became dynamically unstable and the large plasmoids start a horizontal motion, with significant adiabatic compression at play. For none of the constant resistivity finite difference experiments does the global structure reach this point. The least diffusive experiments, likely to experience this evolution, fail to reach very far due to the numerical issues mentioned earlier. Only for the highest diffusivity values are the experiments able to continue for a very long time, and may eventually reach a state where this instability sets in. Rather than continuing the study with this non-standard constant diffusion treatment, we now demonstrate how high order finite difference codes with dedicated hyper-diffusivity treatments do capture these phases more appropriately.

C. Hyper-diffusivity finite difference runs

The stagger code normally operates with high order stencils using 6 grid points, and a constant parameter diffusion operator is not standard practice for highly nonlinear simulations. For this, it is required to use a dedicated high order approach to keep the solution stable in time. In smooth regions, the high order stencil provides a very high accuracy to approximate function shapes and is therefore ideal to handle waves etc., providing very small damping due to correspondingly very low truncation errors. When reaching situations including shocks or current sheets, the high order stencil is a disadvantage as it consequently introduces ringing in physical variables since values are derived on different staggered grids. To compensate for this problem, dedicated diffusion operators are implemented to take direct care of critical situations, maintaining a near smooth structure of the grid values across for instance current sheets and shock fronts.

A fairer test for the finite difference code is therefore to use these optimised diffusion operators when running the experiments. This has been done for a series of different numerical resolutions from 480^2, 960^2, 1920^2, and 3840^2 (the CS-N* series) and in this case no code breakdown ever occurs. The result for the energy evolution is seen in Fig. 15. Here, we show four different quantities. Top left represents the energy plots as seen for a number of the other experiments. This demonstrates energy conservation until $t \approx 255$, which is the time where the current magnitude suddenly increases significantly for the high resolution run. Looking at the magnetic energy, it is noticed that it starts to oscillate after $t \approx 230$. These oscillations represent the big plasma motions seen in the results from the MPI-AMRVAC code discussed above. These oscillations are clearly seen in the kinetic energy shown in the top right panel of the figure. Notice how the different resolution experiments all show the same type of behavior, but that the amplitudes of the oscillations depend on the numerical resolution, with the two highest resolutions being almost on top of each other, while there are clear phase, amplitude and even oscillation period differences relative to the lower resolution experiments. These differences are in part a consequence of the fact that the numerical approach now scales the imposed diffusivity with the actual grid resolution. This implies that the effective diffusion scales with grid resolution and therefore the

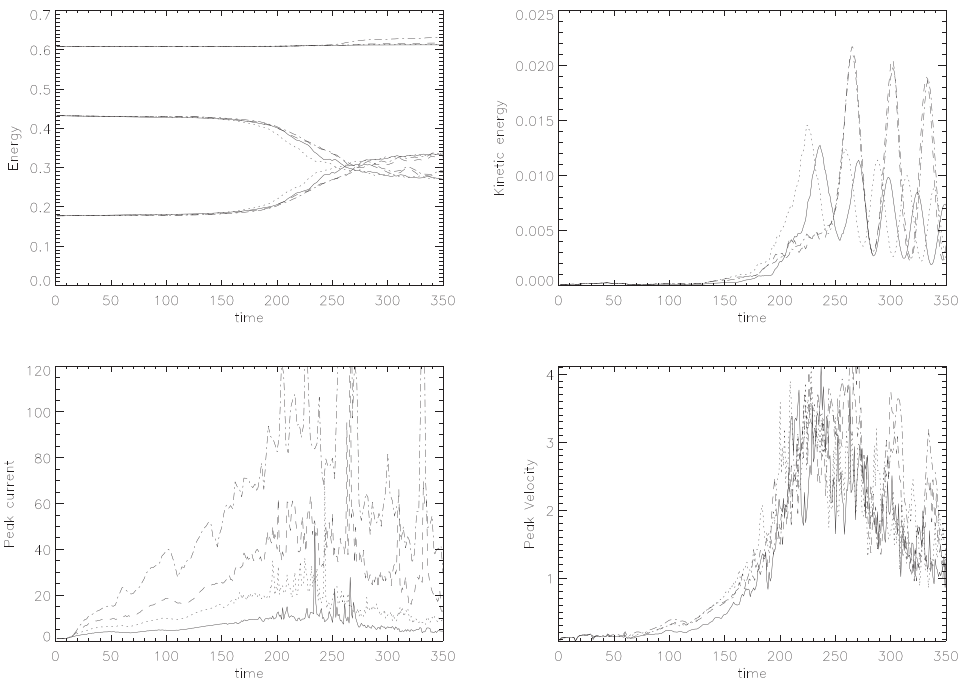

FIG. 15. For the four finite difference runs with hyperdiffusion, differing in the resolution from 480^2 (solid), 960^2 (dot), 1920^2 (dash) to 3820^2 (dash-dot), we show at top left: total energy and magnetic and thermal contributions; top right: kinetic energy; bottom left: peak current; bottom right: peak velocity magnitude.

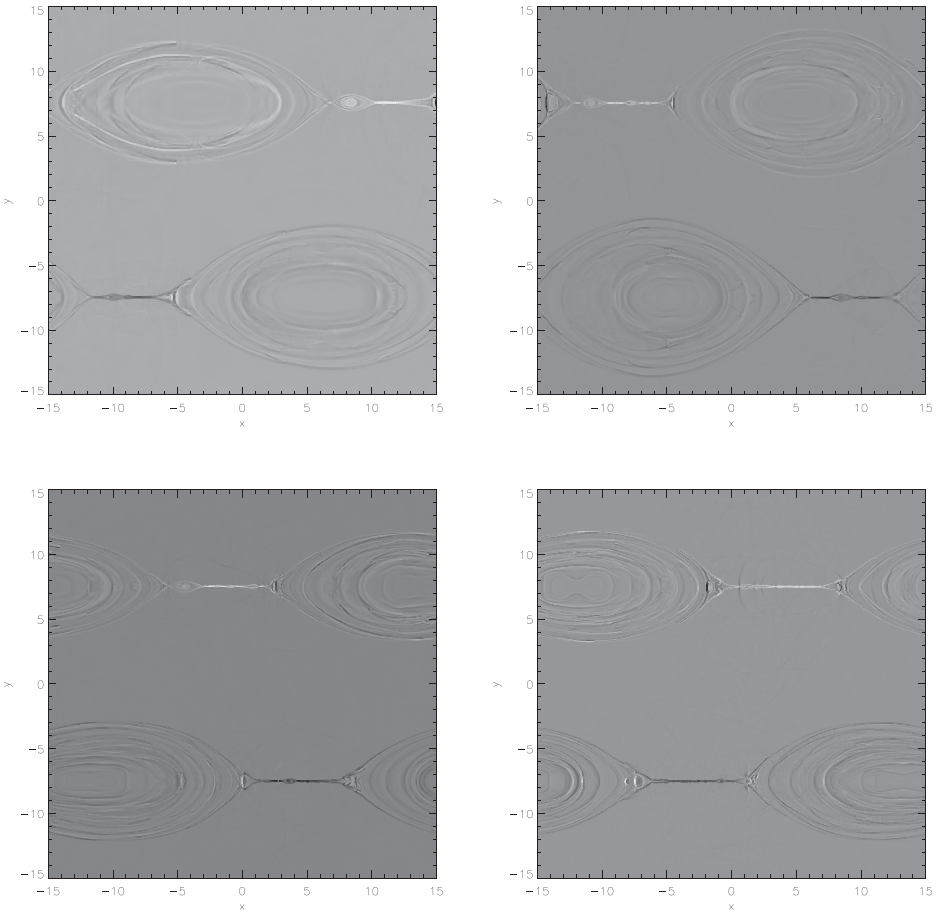

FIG. 16. The four panels show the electric current at $t = 250$ for finite difference experiments with numerical (hyper)diffusion. The panels correspond to different numerical resolutions: 480^2, 960^2, 1920^2, and 3820^2 from top left to bottom right.

experiments also show how the field evolves dependent on the effective Reynolds number of the experiment. The resistivity scaling is most clearly seen in the lower left panel of the figure, which shows the peak current as a function of time for the various experiments. Here the four different curves are clearly seen, obtaining an increasingly higher current density in the developing current sheet as the resolution increases. Finally the lower right panel shows the peak flow velocity in the domain as a function of time. Here only statistically differences between the experiments are seen. This implies that reaching a higher numerical resolution, and by this a shorter length scale across the current sheet, does not imply a higher outflow velocity of the reconnection jet. This value is determined by the large scale values of the magnetic field—the change in the Alfvén velocity is only minor despite the shorter length scales on which the dynamics take place. A comparison of the electric current for the four experiments is shown in Fig. 16.

D. Resistivity scaling

The final comparison between finite difference runs shows how the different energy parameters depend on the imposed resistivity in Fig. 17. This is done for all 1920^2 experiments covering both constant and numerically imposed diffusivity. Only the case with the numerical diffusivity has visible deviations from the total energy conservation. This experiment is also the one that shows the most fluctuating behaviour of the two major contributions (magnetic and thermal) in the later phases of the experiment, correlating to the large plasmoid motions discussed earlier. From the peak current and velocity it is again clear that only

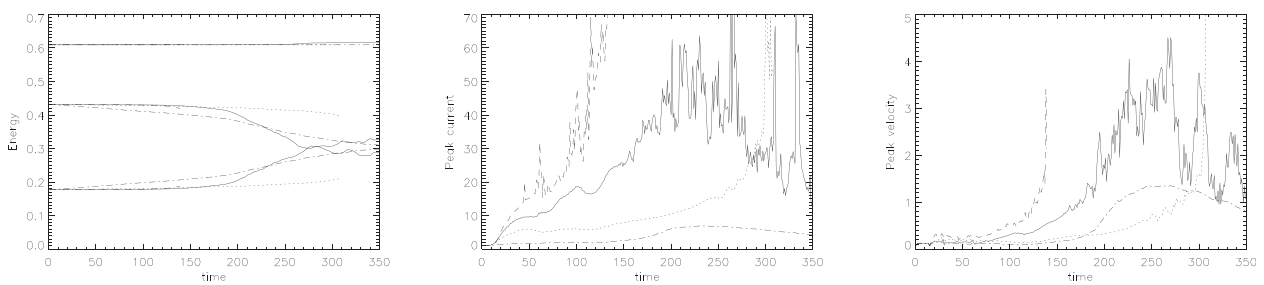

FIG. 17. The figures show the results of running finite difference experiments at 1920^2 resolution for different values of the resistivity. Full line is hyper resistivity, dotted-dashed line is constant $\eta = 0.01$, dotted line is $\eta = 0.001$ and dashed line is for $\eta = 0.0001$. Far left represents the energy, middle peak current and right peak velocity.

two experiments managed to run for the full time series, namely, the one with the highest constant resistivity and the numerical diffusion approach. Overall though, this comparison shows clear analogy with the results at fixed resolution of the finite volume runs, collected in Fig. 10.

V. FLIP-MHD SIMULATIONS

A third means to solve the (visco-)resistive MHD equations presented here uses an updated variant of the FLIP-MHD code,[24] which was also used in the original work that first pointed out the self-feeding, turbulent magnetic reconnection regime.[13] This code employs a PIC type means to discretize the governing equations, where in essence a mixed Eulerian-Lagrangian approach is taken: next to a grid of fixed size, we also have a certain number of fluid elements (serving as "particles") to evolve. Their combination acts as an effective resolution, and we report here on results where a 240×240 grid is combined with initially 4×4 particles per cell, serving as a 960×960 resolution simulation. The basic algorithm[24] involves the interpolation of particle data (mass, momentum, internal energy, position, and magnetization) to an underlying grid of quadrilaterals using a shape function for each particle. When going from particles to the grid, it is to be noted that a staggering is employed for the MHD variables on the grid. One then solves a (second-order) finite-difference approximation to the MHD equations written in Lagrangian form on this grid, which thereby gets distorted by the plasma motion. In this phase, particle positions remain geometrically fixed to distorted cell shapes, and one next interpolates the variations of the fluid properties during the time step from the grid back to the particles. A new grid is then created, filled with information based on the displaced particles, and a new cycle starts from the new grid plus particle population. The regenerated grid in each cycle is here taken as the initial Cartesian grid, and particles therefore seemingly move through this grid. The FLIP-MHD method is designed to minimize diffusion by using the Lagrangian formulation employing primitive variables like velocity and internal energy, and in the employed variant does not guarantee total energy conservation, as will be evident further on. With this FLIP-MHD approach (which advances fluid elements in a similar fashion as PIC codes), we perform two sets of computations, one set of unperturbed experiments for ideal and resistive MHD regimes, and another imposing the perturbation in resistive runs. The parameters are summarized in Table III.

TABLE III. The parameters for the FLIP-MHD runs. The leftmost column serves to label the various experiments.

Run	ψ	η (μ)	$N_x \times N_y$ (particles)	Comments
FM-Id1	0	0 (0)	240×240 (4×4)	Ideal, no perturbation
FM-Anp	0	0.01 (0.001)	240×240 (4×4)	Resistive, no perturbation
FM-Bnp	0	0.001 (0.001)	240×240 (4×4)	
FM-Cnp	0	0.0001 (0.001)	240×240 (4×4)	
FM-A	0.1	0.01 (0.001)	240×240 (4×4)	Resistive, perturbed
FM-B	0.1	0.001 (0.001)	240×240 (4×4)	
FM-C	0.1	0.0001 (0.001)	240×240 (4×4)	

Figure 18 collects the FLIP-MHD results for the unperturbed experiments. The energy plot (left panel) can be compared with Figure 11 for the finite difference realization, and confirms that in this (essentially 1D) case, both the ideal and resistive evolutions agree with all previous findings. While in the ideal run, this experiment tests whether the discretization can maintain an equilibrium configuration, the resistive runs demonstrate how internal energy increases at the expense of magnetic energy while keeping total energy constant, with the exchange in an amount consistent with the occurring Ohmic heating. The second and third panels show the maximal current evolution for all four cases, as well as the maximal velocity in the simulations. The current value for the ideal case is kept nearly constant, with some small oscillatory variation especially at early times. For the resistive, unperturbed cases, the maximal current value drops off through the physical Ohmic-heating mediated diffusion (compare with the maximal current evolution for the unperturbed cases using MPI-AMRVAC also shown in Figs. 1–6). The maximal velocity is seen to oscillate initially, to then settle on a (low) value dependent on the resistivity. Especially these initial oscillations are typical for the PIC-like approach where the mutual interpolations between grid and particles cause some artificial, transient behavior and can possibly give rise to ringing (and in the worst case, trigger a numerical instability).[25] Note that the right panel quantifies the instantaneous maximal velocity, the overall kinetic energy levels are again negligible, and compare favorably with the values given for the MPI-AMRVAC and Stagger results. For the ideal, unperturbed run, the FLIP-MHD approach ultimately settles on a kinetic energy averaged over the box size of order $\mathcal{O}(10^{-9})$.

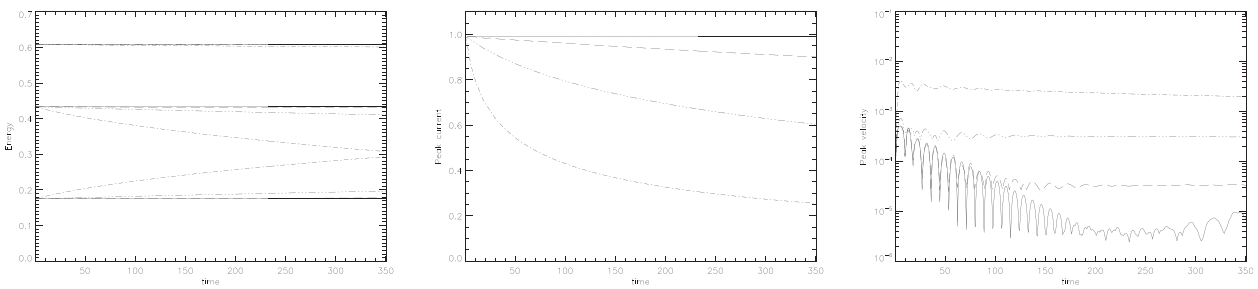

FIG. 18. The figures show the results of running particle-based, unperturbed experiments at 240^2 resolution, with initially 4×4 particles per cell. The plots collect results for the ideal $\eta = 0$ case (solid), as well as for different values of the resistivity, dashed line is constant $\eta = 0.01$, dashed-dotted line is $\eta = 0.001$ and dashed-triple dotted line is for $\eta = 0.0001$. Far left represents the energy (total, magnetic, and internal), middle peak current and right maximal velocity.

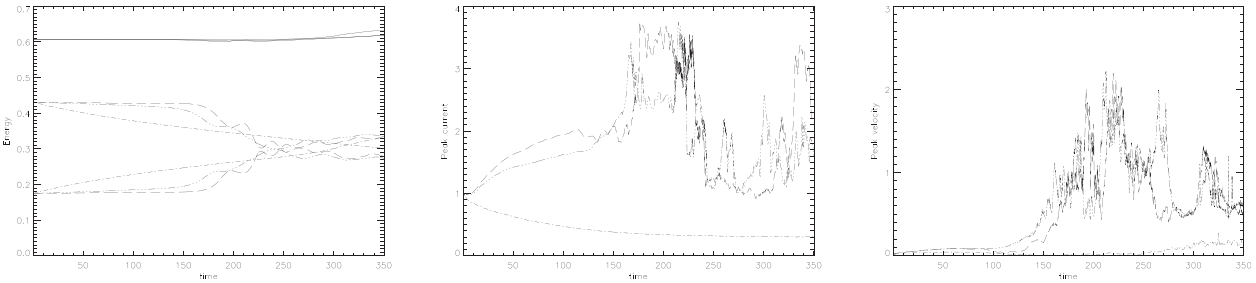

FIG. 19. The figures show the results of running particle-based, perturbed experiments at 240^2 resolution, with initially 4×4 particles per cell. The plots collect results for different values of the resistivity, dashed line is constant $\eta = 0.01$, dashed-dotted line is $\eta = 0.001$, and dashed-triple dotted line is for $\eta = 0.0001$. Far left represents the energy (total, magnetic, and internal), middle peak current and right peak velocity.

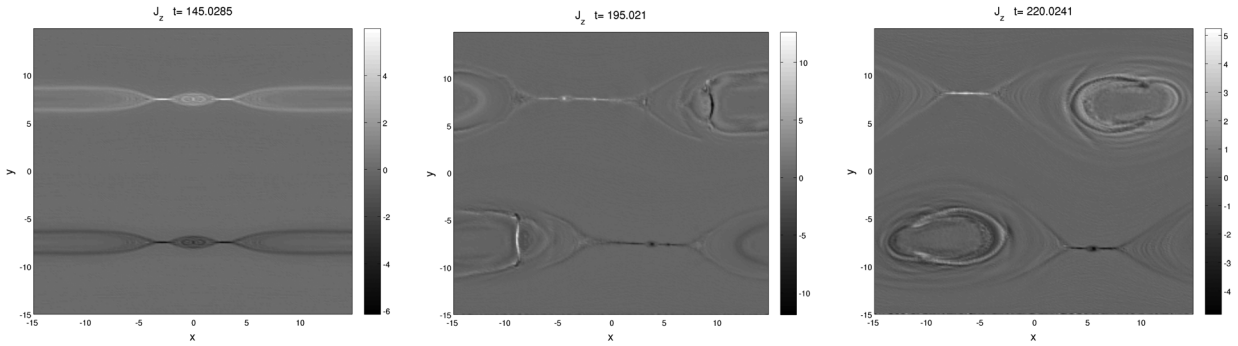

FIG. 20. The current distribution for a perturbed FLIP-MHD run at $\eta = 0.0001$, at selected times.

The particle-based simulations for the perturbed, resistive experiments listed in Table III are quantified in terms of energy evolution, maximal current and velocity in Figure 19. This plot can be compared with Fig. 17 for the finite difference runs (where runs with constant resistivity prescriptions not always managed to cover the full time period), and with the MPI-AMRVAC runs as shown in Fig. 2 for $\eta = 0.01$, Fig. 3 for $\eta = 0.001$, and Fig. 6 for $\eta = 0.0001$. A first observation is that the particle-based method can handle the uniform (visco-)resistive evolutions, and confirms the finite volume based findings: while at $\eta = 0.01$, the perturbed run behaves similar to the unperturbed run with the same resistivity, the higher Reynolds number cases show the clear transition to the later phase where compressive events enhance the exchange of magnetic to internal energy beyond that realized by mere Ohmic heating. The perturbed FLIP-MHD runs (FM-A, FM-B, FM-C) do also suffer from non-exact energy conservation, most pronounced in the last roughly 50 time units. The maximal current values and velocity values shown in the middle and right panel of Fig. 19 also show the transition when η decreases to the island-dominated chaotic phase, with peak velocities up to Alfvénic values, in correspondence with the MPI-AMRVAC findings, as well as with the Stagger results when employing (necessary for stabilization) hyperdiffusion prescriptions. The run for $\eta = 0.01$, which with MPI-AMRVAC ultimately evolved similarly to its unperturbed equivalent, here does show some deviations at later times as well, as seen in the small fluctuations in peak current, with a corresponding increase in velocity fluctuations. This may be related to the ringing mentioned earlier, although it does not lead to numerical instability in the timeframe shown. The trend with decreasing η values is obvious though, with the chaotic phase appearing at η values in between 0.01 and 0.001. FLIP-MHD snapshots of the current distribution in this chaotic phase, for $\eta = 0.0001$ at times $t \approx 145$, 195, 220, are depicted in Fig. 20. They agree well with the evolutions found using MPI-AMRVAC, or Stagger runs employing hyperdiffusion. Overall, quantitative differences exist in the overall timings and peak values reached with the different methods, and resolution studies using the FLIP-MHD approach alone similarly find only qualitative agreement.

VI. CONCLUSIONS

In this paper, we studied a 2D double periodic, double current system, which depending on the prevailing values of resistivity can enter a reconnection regime, ultimately characterized by secondary tearing events and compressive island interactions. We simulated the long-term evolution with a large variety of commonly adopted discretizations, allowing us to draw the following conclusions.

When a critical magnetic Reynolds number is reached, the nonlinearly perturbed current layers enter a regime where the centrally collapsed current layers become liable to additional plasmoid formation. For lower values of the resistivity parameter η, this is accompanied with order of magnitude increases in the maximal peak currents reached, and secondary islands form erratically and coalesce with the larger plasmoids. This transition happens on longer timescales, at a few hundred Alfvénic time units, and eventually left-right symmetry gets broken and the growing, large plasmoids start an

oscillatory sideways motion where compressive heating dominates resistive heating. All discretizations (finite volume, high order finite difference, particle-based) demonstrate these overall trends and agree on the different evolutionary phases. At the same time, none of the schemes can demonstrate true (strong) convergence in this chaotic phase, as peak current values continue to rise with resolutions adopted, and the details in when secondary islands appear, their overall sizes reached, and the dynamics of their coalescence with other plasmoids vary from scheme to scheme, and with resolution when adopting a single discretization strategy.

We stressed the importance of respecting overall conservation of energy, which proves particularly challenging to the late term stages with compressive heating and chaotic island formations. All discretizations (finite volume based, higher order finite difference, and particle based) can demonstrate the correct (1D) behavior with *unperturbed* ideal to resistive tests, where full numerical convergence can be demonstrated. The more relevant, perturbed 2D resistive tests show that at resistivity values of 0.001 and lower, deviations from total energy conservation can occur in finite difference runs exploiting primitive variable updates directly, or in PIC-like treatments which do not enforce total energy conservation exactly either. Finite volume treatments with up to third order accuracy do well on all aspects, and can use uniform resistivity values and no explicit viscous terms to capture the various evolutionary phases, while viscous terms were included in finite difference and particle-based runs. Finite difference runs need to exploit hyperdiffusion (visco-resistive) prescriptions, and need a correspondingly larger resolution, to agree on the transition to the late term stages. When insisting on uniform resistivity prescriptions, the chaotic islands can be resolved only for early times in a finite difference approach, while a trend for smaller secondary island sizes with larger stencils was found. Employing hyperdiffusion resolves all numerical issues for finite difference treatments, and allows to draw definite conclusions on the velocity evolutions associated with the reconnecting sheets. Their hyperdiffusion makes it less straightforward to quantify the precise (time and space evolving) Reynolds number regime simulated. Particle based methods can employ a grid which is much coarser than the other approaches, as along as enough particles per cell are taken initially. At the same time, one can note that the means for magnetic monopole control differ greatly between the three approaches, where staggered variables ensure zero magnetic field divergence to machine precision, while the MPI-AMRVAC runs merely controlled monopoles using a diffusive treatment to damp monopole errors.

In summary, this study has highlighted the enormous challenges faced when addressing high Reynolds number evolutions using contemporary discretization schemes. Note that the values for the resistivity parameter η explored here translate to magnetic Reynolds numbers of order 1000 to at most order 10000. This is to be contrasted with recent studies where even higher Reynolds number regimes are handled. We argue that such numerical studies of reconnection should provide all details on the algorithmic approaches used for stably simulating chaotic phases, and complement it with tests where true convergence properties hold or cease to be valid. Indeed, even at the relatively modest Reynolds numbers used here, our comparison can at best claim qualitative agreement between various methods and within resolution studies in a fixed discretization. In follow up work, we intend to augment this study with complementary quantifications of the reconnection rates and study the differences in the magnetic topological evolutions (X- versus O-point creation and destruction) which typify the later chaotic stages. There again, underlying discretization strategies can influence the results, here already exposed using the overall energetics. In the future, extensions to 3D and the corresponding resolution requirements, excursions from visco-resistive to Hall MHD regimes, can all be explored.

ACKNOWLEDGMENTS

We acknowledge financial support from the EC FP7/2007-2013 Grant Agreement SWIFF (No. 263340) and from project GOA/2009/009 (KU Leuven). This research has been funded by the Interuniversity Attraction Poles Programme initiated by the Belgian Science Policy Office (IAP P7/08 CHARM). Part of the simulations used the infrastructure of the VSC-Flemish Supercomputer Center, funded by the Hercules Foundation and the Flemish Government-Department EWI. Another part of the simulations was done at the former Danish Center for Scientific Computing at Copenhagen University which is now part of DeIC Danish e-Infrastructure Cooperation.

[1]E. N. Parker, J. Geophys. Res. **62**, 509–520, doi:10.1029/JZ062i004p00509 (1957).
[2]H. E. Petschek, in *Physics of Solar Flares*, edited by W. N. Hess (NASA, Washington, DC, 1964), NASA SP-50, pp. 425–439 (1964).
[3]M. Hesse, J. Birn, and S. Zenitani, Phys. Plasmas **18**, 042104 (2011).
[4]J. Birn, M. Hesse, and S. Zenitani, Phys. Plasmas **18**, 111202 (2011).
[5]J. Birn, J. E. Borovsky, M. Hesse, and K. Schindler, Phys. Plasmas **17**, 052108 (2010).
[6]H. Baty, E. R. Priest, and T. G. Forbes, Phys. Plasmas **16**, 060701 (2009).
[7]J. Birn, J. F. Drake, M. A. Shay, B. N. Rogers, R. E. Denton, M. Hesse, M. Kuznetsova, Z. W. Ma, A. Bhattacharjee, A. Otto, and P. L. Pritchett, J. Geophys. Res. **106**, 3715–3719, doi:10.1029/1999JA900449 (2001).
[8]J. Birn, K. Galsgaard, M. Hesse, M. Hoshino, J. Huba, G. Lapenta, P. L. Pritchett, K. Schindler, L. Yin, J. Büchner, T. Neukirch, and E. R. Priest, Geophys. Res. Lett. **32**, L06105, doi:10.1029/2004GL022058 (2005).
[9]J. Birn, J. E. Borovsky, and M. Hesse, Phys. Plasmas **19**, 082109 (2012).
[10]J. Birn, M. Hesse, and K. Schindler, Phys. Plasmas **13**, 092117 (2006).
[11]J. P. Goedbloed, R. Keppens, and S. Poedts, *Advanced Magnetohydrodynamics* (Cambridge University Press, Cambridge, 2010).
[12]R. Keppens, Z. Meliani, A. J. van Marle, P. Delmont, A. Vlasis, and B. van der Holst, "Parallel, grid-adaptive approaches for relativistic hydro and magnetohydrodynamics," J. Comput. Phys. **231**, 718 (2012).
[13]G. Lapenta, Phys. Rev. Lett. **100**, 235001 (2008).
[14]A. Bhattacharjee, Y.-M. Huang, H. Yang, and B. Rogers, Phys. Plasmas **16**, 112102 (2009).
[15]Y.-M. Huang and A. Bhattacharjee, Phys. Rev. Lett. **109**, 265002 (2012).
[16]S. D. Baalrud, A. Bhattacharjee, Y.-M. Huang, and K. Germaschewski, Phys. Plasmas **18**, 092108 (2011).
[17]N. F. Loureiro, R. Samtaney, A. A. Schekochihin, and D. A. Uzdensky, Phys. Plasmas **19**, 042303 (2012).
[18]H. Baty, Phys. Plasmas **19**, 092110 (2012).
[19]J. Birn and M. Hesse, J. Geophys. Res. **106**, 3737–3750, doi:10.1029/1999JA001001 (2001).
[20]M. Čada and M. Torrilhon, "Compact third-order limiter functions for finite volume methods," J. Comput. Phys. **228**, 4118 (2009).

[21]A. Nordlund and K. Galsgaard, "A 3D MHD code for parallel computers," Technical Report Niels Bohr Institute, 1997..
[22]A. G. Kritsuk, A. Nordlund, D. Collins, P. Padoan, M. L. Norman, T. Abel, R. Banerjee, C. Federrath, M. Flock, D. Lee, P. S. Li, W.-C. Müller, R. Teyssier, S. D. Ustyugov, C. Vogel, and H. Xu, "Comparing numerical methods for isothermal magnetized supersonic turbulence," Astrophys. J. **737**, 13 (2011).
[23]G. Baumann, K. Galsgaard, and A. Nordlund, "3D solar null point reconnection MHD simulations," Solar Phys. **284**, 467 (2013).
[24]J. U. Brackbill, "FLIP MHD: A particle-in-cell method for magnetohydrodynamics," J. Comput. Phys. **96**, 163 (1991).
[25]J. U. Brackbill, "The ringing instability in particle-in-cell calculations of low-speed flow," J. Comput. Phys. **75**, 469 (1988).